RESEARCH ARTICLE | JUNE 12 2024

## Transferable GeSn ribbon photodetectors for high-speed short-wave infrared photonic applications • 🕬

Special Collection: Developing SiGeSn Technology: Materials and Devices

Haochen Zhao 📵 ; Suho Park; Guangyang Lin; Yuying Zhang 📵 ; Tuofu Zhama; Chandan Samanta 💩 ; Lorry Chang 💿 ; Xiaofeng Zhu 💿 ; Xu Feng; Kevin O. Díaz-Aponte 💿 ; Lin Cong 💿 ; Yuping Zeng 🖼 💿



J. Vac. Sci. Technol. B 42, 042205 (2024) https://doi.org/10.1116/6.0003561





### Articles You May Be Interested In

GeSn p-i-n photodetectors with GeSn layer grown by magnetron sputtering epitaxy

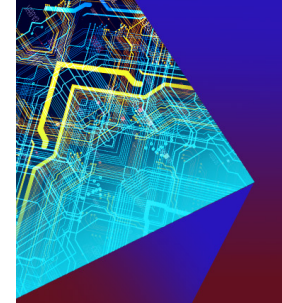
Appl. Phys. Lett. (January 2016)

SiGeSn buffer layer for the growth of GeSn films

J. Appl. Phys. (July 2023)

High-quality  $Ge_{1-x}Sn_x$  (x = 0–0.11) realized by UHV-CVD using  $Ge_2H_6$  and  $SnCl_4$ : Materials growth, structural/optical properties, and prototype IR photodetectors

APL Mater. (July 2024)



# **APL Electronic Devices**

Open, quality research for the broad electronics community

Meet the new Editor-in-Chief



**Learn More** 



Cite as: J. Vac. Sci. Technol. B 42, 042205 (2024); doi: 10.1116/6.0003561 Submitted: 20 February 2024 · Accepted: 15 May 2024 · Published Online: 12 June 2024







Haochen Zhao, 1 D Suho Park, 1 Guangyang Lin, 1 Yuying Zhang, 2 D Tuofu Zhama, 1 Chandan Samanta, 1 D Lorry Chang, 1 📵 Xiaofeng Zhu, 1 📵 Xu Feng, 3 Kevin O. Díaz-Aponte, 4 📵 Lin Cong, 4 📵 and Yuping Zeng 1.a.) 📵

#### **AFFILIATIONS**

- Department of Electrical and Computer Engineering, University of Delaware, Newark, Delaware 19716
- <sup>2</sup>Department of Materials Science and Engineering, University of Delaware, Newark, Delaware 19716
- <sup>3</sup>Surface Analysis Facility, University of Delaware, Newark, Delaware 19716
- Department of Physics and Engineering, Delaware State University, Dover, Delaware 19901

Note: This paper is part of the 2024 Special Topic Collection on Developing SiGeSn Technology: Materials and Devices.

a)Author to whom correspondence should be addressed: yzeng@udel.edu

ABSTRACT

We experimentally demonstrate a low-cost transfer process of GeSn ribbons to insulating substrates for short-wave infrared (SWIR) sensing/ imaging applications. By releasing the original compressive GeSn layer to nearly fully relaxed state GeSn ribbons, the room-temperature spectral response of the photodetector is further extended to 3.2 µm, which can cover the entire SWIR range. Compared with the as-grown GeSn reference photodetectors, the fabricated GeSn ribbon photodetectors have a fivefold improvement in the light-to-dark current ratio, which can improve the detectivity for high-performance photodetection. The transient performance of a GeSn ribbon photodetector is investigated with a rise time of about 40 µs, which exceeds the response time of most GeSn (Ge)-related devices. In addition, this transfer process can be applied on various substrates, making it a versatile technology that can be used for various applications ranging from optoelectronics to large-area electronics. These results provide insightful guidance for the development of low-cost and high-speed SWIR photodetectors based on Sn-containing group IV low-dimensional structures.

Published under an exclusive license by the AVS. https://doi.org/10.1116/6.0003561

#### I. INTRODUCTION

Short-wave infrared (SWIR,  $1.5-3.0 \mu m$ )<sup>1</sup> photodetectors (PDs) are of significant importance in a wide variety of practical applications such as spectral sensing,2 chemical/biological detection,3 medical imaging,4 and optical communications.5,6 Most of the SWIR PDs currently dominating the market are based on group III-V semiconducting compounds (e.g., InGaAs and InSb), along with a few specific material systems such as HgCdTe and other group II-VI semiconductors. 7-9 However, the scarcity of group III/V elements, high-cost growth processes, and low compatibility with existing mainstream silicon (Si) complementary metaloxide-semiconductor (CMOS) technologies make it challenging to further extend them to everyday applications. 10 Recently, group IV material GeSn has emerged as a novel material platform for SWIR

applications, which can also be monolithically integrated into wellestablished and high-yield Si integrated circuits to reduce cost. 11,12 Recent studies have indicated that by incorporating more than ~8%  $\alpha$ -tin (Sn) into Ge, the bandgap transition of GeSn can shift from indirect to direct, consequently leading to an enhancement of the absorption coefficient and increased efficiency in light emission. 13,14 By increasing the Sn composition, the bandgap of GeSn can be extended from the SWIR, mid-wave infrared (MWIR) range  $(3-8 \mu m)$ , and even into the long-wave infrared (LWIR) range  $(8-14\,\mu\text{m})^{15}$  However, the surface free energy of Sn is much lower than that of Ge, and the thermal equilibrium solubility of  $\alpha$ -Sn in Ge is as low as 1%, 16 leading to Sn segregation during epitaxial growth, which brings challenges to the formation of high-quality GeSn alloys.<sup>17</sup> Due to the recent advancements in chemical vapor

deposition (CVD), 18,19 low-temperature molecular beam epitaxy (MBE),<sup>20,21</sup> and sputtering technique,<sup>22,23</sup> GeSn alloys with Sn content up to 33% have been achieved. 24 Various GeSn-based PDs have been demonstrated to have extended photodetection range up to 4.6  $\mu$ m<sup>25</sup> and enhanced quantum efficiency,<sup>26</sup> which has made possible the development of a new generation of SWIR photonics candidates.

GeSn epitaxial layers grown on Ge/Si virtual substrates accompany indispensable biaxial compressive strains due to the large lattice mismatch ( $\sim$ 15%) between Ge and  $\alpha$ -Sn.<sup>2</sup> Unfavorable biaxial compressive strain retards the increase in the lattice constant, thereby impeding the reduction in the bandgap energy.<sup>28</sup> Consequently, a higher incorporation of Sn is required to achieve the desired absorption edge. For the growth of GeSn with high Sn composition, lowering the growth temperature is necessary to avoid nonequilibrium growth conditions. However, the low growth temperature can maximize the difference in the adatom mobility between Ge and Sn, potentially causing S-K mode growth, as well as the occurrence of point and stacking fault defects due to amorphous Ge.<sup>29</sup> These comprehensive issues result in GeSn PD generating a high dark current, which deteriorates optoelectronic performance due to the low signal-to-noise ratio. 10 A few approaches have been proposed to eliminate biaxial compressive strain, such as graded GeSn buffer technologies<sup>30</sup> and wafer bonding technologies.<sup>3</sup> However, since these GeSn PDs are fabricated on rigid or fixed substrates, they lack the required flexibility to be applied to a wide range of platforms.

In this article, we use a low-cost epitaxial transfer scheme for integrating GeSn layers on SiO<sub>2</sub>/Si substrates for high-performance GeSn PDs. By releasing the original compressive GeSn layer to nearly fully relaxed state GeSn ribbons, the room-temperature spectral response of the PD is further extended to  $3.2 \mu m$ , which can cover the entire SWIR range. Furthermore, the prepared GeSn ribbon PD can improve the I<sub>light</sub> to I<sub>dark</sub> current ratio by about fivefold under the same light illumination compared with the GeSn as-grown PD. We also used a variety of experimental tools to study the crystalline quality, lattice strain uniformity, and metal contact for the GeSn material after the transfer process. Our work may open a new avenue for low-cost and high-performance SWIR detection based on GeSn-related group IV semiconductor materials.

#### II. EXPERIMENT

#### A. Epitaxy of GeSn and Ge buffer layer

Ge and GeSn materials were grown using a Veeco/EPI Model 620 solid source MBE system with a base pressure of  $1 \times 10^{-10}\,\mathrm{Torr.}$  GeSn and Ge buffer layers were epitaxially grown on 3 in. p-type silicon (001) wafers. The Si substrate cleaning procedure and Ge buffer layer growth process can be found in our previous work.<sup>32</sup> After completing the growth of the Ge buffer layer (530 nm), the substrate temperature was then lowered to 150 °C to avoid Sn segregation and maximize Sn incorporation. A 330 nm GeSn layer with an Sn content of 10.5% was grown on the Ge buffer layer within 7 h.

#### B. Transfer process of GeSn ribbons

A two-step etching process was used in this work to form suspended GeSn ribbons. Prior to the etching process, the as-grown GeSn samples were successively immersed in acetone and isopropyl alcohol (IPA) for 10 min by ultrasound cleaning to remove organic compounds and other impurity elements. The samples were then immersed in a mixture solution (HF/HCl/  $H_2O = 4/25/171$ ) for 5 min to remove oxides. Positive photoresist (PR) S1818 line patterns were formed on the surface of the as-grown GeSn samples by lithography. The GeSn layer together with underneath Ge buffer layer was then pattern etched into nanoribbons using a mixture solution (H<sub>3</sub>PO<sub>4</sub>/CH<sub>3</sub>COOH/  $HNO_3/H_2O = 72/3/3/22$ ). The etching rate of the solution varies with Sn concentration. The etching rates of 10% GeSn and Ge buffer layers were tested to be around 30 and 60 nm/min, respectively. Since the solution does not etch the Si substrate, the Si substrate can be used as an etch stop layer. The optical image after the first etching can be seen in Fig. 1(b). To release the GeSn nanoribbons from the source substrate, the Ge buffer layer was selectively etched by  $(NH_4OH/H_2O_2/H_2O = 2/1/160)$ solution for ~5 min. After the selective etching of Ge buffer, the photoresist was removed by N-methyl-2-pyrrolidone (NMP) in a water bath at 80 °C. The optical image of the sample surface after selective wet etching and removal of PR can be seen in Fig. 1(d). With this recipe, suspended GeSn nanoribbons were fabricated. After acquisition of the suspended GeSn microstructures, a polydimethylsiloxane (PDMS) slab was used to pick  $_{\odot}$ up GeSn. During the transfer process, residues from the Ge of buffer layer may remain on the back surface of GeSn ribbons. Figure 1(f) shows several GeSn ribbons on the PDMS. To remove any potential residues on the backside, the PDMS slab 8 with GeSn ribbons was then immersed into the selective etching solution again for 1 min to remove residual Ge and finally transfer the GeSn onto a 260 nm SiO<sub>2</sub>/Si substrate forming the GeSnOI structure, as shown in Fig. 1(h).

#### C. Fabrication process of metal-semiconductor-metal **PDs**

In this work, all GeSn-related devices were fabricated by photolithography pattering and metallization. Ti/Au (80/50 nm) metal stack was deposited by e-beam evaporation to form electrical contacts and then followed by a standard lift-off process. Surface oxides were removed with 12.5% dilute hydrochloric acid (HCl) prior to metal deposition to avoid the effect of oxides on the formation of ohmic contacts.

#### III. METHODOLOGY

#### A. Characterization of GeSn/Ge epilayer and GeSn ribbons

The surface morphology and microstructure of the films were characterized by an atomic force microscope (AFM) and a transmission electron microscope (TEM). The final thickness of the GeSn and Ge buffer layer was determined using TEM Talos F200C in the cross-sectional geometry. The x-ray diffractor (XRD) (004) reflection  $\omega - 2\theta$  rocking-curve scan and (224) reciprocal space

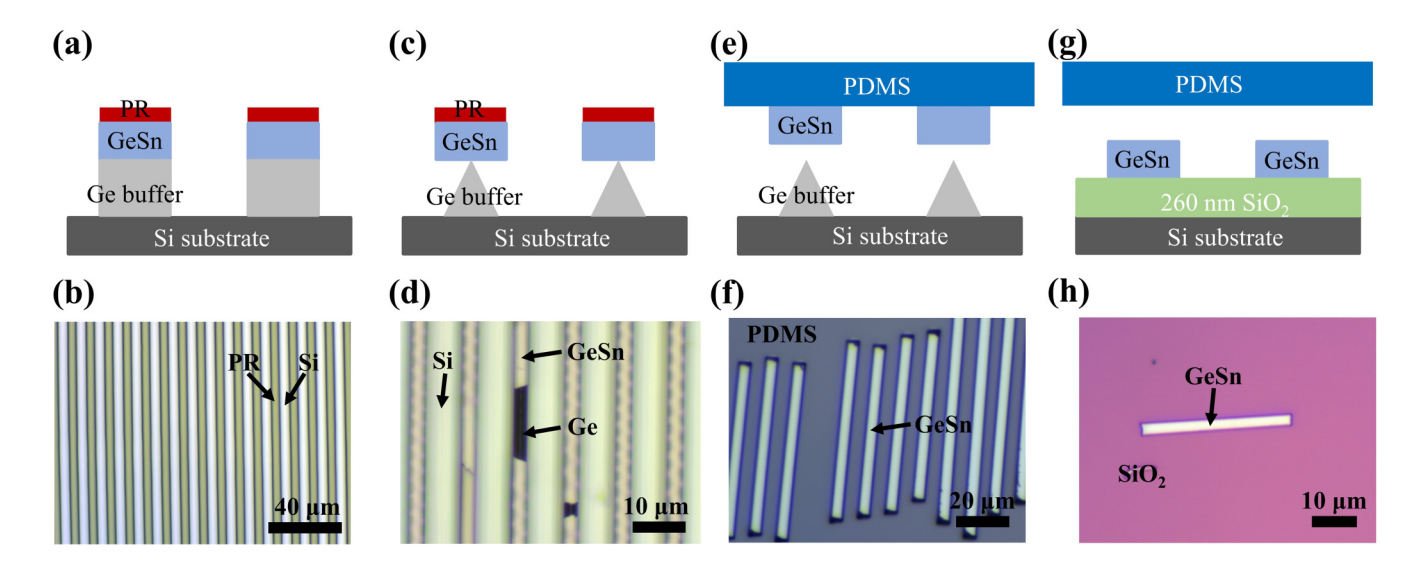


FIG. 1. Schematic diagram and corresponding optical images of the main process flow for the fabrication of GeSn ribbons and the transfer to the  $SiO_2/Si$  substrate: (a) nonselective wet etching (Si substrate as the etching stop layer), (b) optical image of the sample surface after nonselective wet etching, (c) fabrication of suspended GeSn microstructures on Ge by explored wet etching methods, (d) optical image of the sample surface after selective wet etching and removal of PR, (e) picking up GeSn ribbons by the PDMS slab, (f) optical image of several GeSn ribbons on PDMS, (g) transfer of GeSn ribbons onto the insulator substrate and (h) optical image of the GeSn ribbon on the  $SiO_2/Si$  substrate.

mapping (RSM) taken by Rigaku SmartLab II were used to evaluate the crystal quality, Sn content, and strain level of the GeSn film. GeSn layer thickness and Sn composition were also validated by time-of-flight secondary ion mass spectrometry (ToF-SIMS) measurements. Raman measurement was performed at room temperature using a Horiba LabRAM Raman spectrometer with a 532 nm laser and equipped with 1800/mm diffraction grating. The incident light was focused on the sample surface with a diameter of  $1\,\mu\mathrm{m}$  by using a microscope objective with a magnification of 100×. The laser power was kept at low lever  $\sim\!2.2\,\mathrm{mW}$  to avoid the GeSn layer heating effect.

# B. Photocurrent measurements for GeSn-related MSM PDs

A1550 nm tunable laser Ando AQ4321A was used as the light source for photocurrent measurements. The 1550 nm light was coupled to an SMF fiber change to a single-mode optical fiber (SMF) ( $10\,\mu m$  core/ $125\,\mu m$  cladding) and finally irradiated normally onto the device. The device bias with a Keithley source meter was fixed at a homemade probe station, and the fiber position was controlled by a Thorlabs 3-axis fiber alignment stage. For temporal 1550 nm optical response measurement, a 1550 nm tunable laser Ando AQ4321A with internal chopper mode was used to generate pulsed 1550 nm laser light signals at different frequencies in the range from 200 Hz to 300 kHz. The photovoltage signals were generated and recorded and output with an oscilloscope. Spectral photoresponse measurements were performed in a Fourier transform infrared spectrometer (FTIR) Thermo Fisher iS50R with an amplitude step scan mode. More details can be found in previous studies.  $^{32}$ 

#### IV. RESULTS AND DISCUSSION

#### A. Structure and morphology analysis

To investigate the GeSn surface morphology, an AFM scan is conducted. As shown in Fig. 2(a), the surface of the as-grown sample is very smooth exhibiting a root-mean-square (RMS) roughness of 0.49 nm. Figure 2(b) shows the cross-sectional TEM image of the GeSn layer (330 nm thick) epitaxially grown on a Ge buffer layer (530 nm thick) on a bulk Si wafer with distinct interfaces of Ge buffer/Si and GeSn/Ge buffer. A large number of misfit dislocations can be found at the interface between the LT-Ge buffer and Si substrate. However, the mismatch dislocation is restricted in LT-Ge buffer and there is almost no threading dislocation extending upward, which confirms the high quality of the top GeSn layer. Figure 2(c) is a selected area electron diffraction (SAED) pattern of the GeSn and Ge buffer layers, which shows that both the GeSn and Ge buffer layers are in a single-crystalline state. Figure 1(d) shows a zoomed-in HRTEM image of the interface between the GeSn and Ge buffer layers. The fast Fourier transformation (FFT) pattern inserted in Fig. 2(d) of the GeSn layer and top Ge buffer layer shows coherent growth of the top Ge buffer and the GeSn layer. To quantitatively characterize the Sn concentration and strain in the GeSn layer, XRD-RSM around the asymmetric (224) reflection was obtained, as shown in Fig. 2(e). In the RSM, the intensity of the diffracted beam is depicted as the contour of equal intensity, which is a function of the reciprocal lattice vectors along the [110]  $(Q_{/\!/})$  and [001]  $(Q_{\perp})$  directions. From upper contour peak to lower contour peak in RSM are from the diffraction of the Si substrate, Ge buffer, and GeSn layer, respectively. The red dashed line between the Si peaks (upper right) and Ge buffer peaks (center)



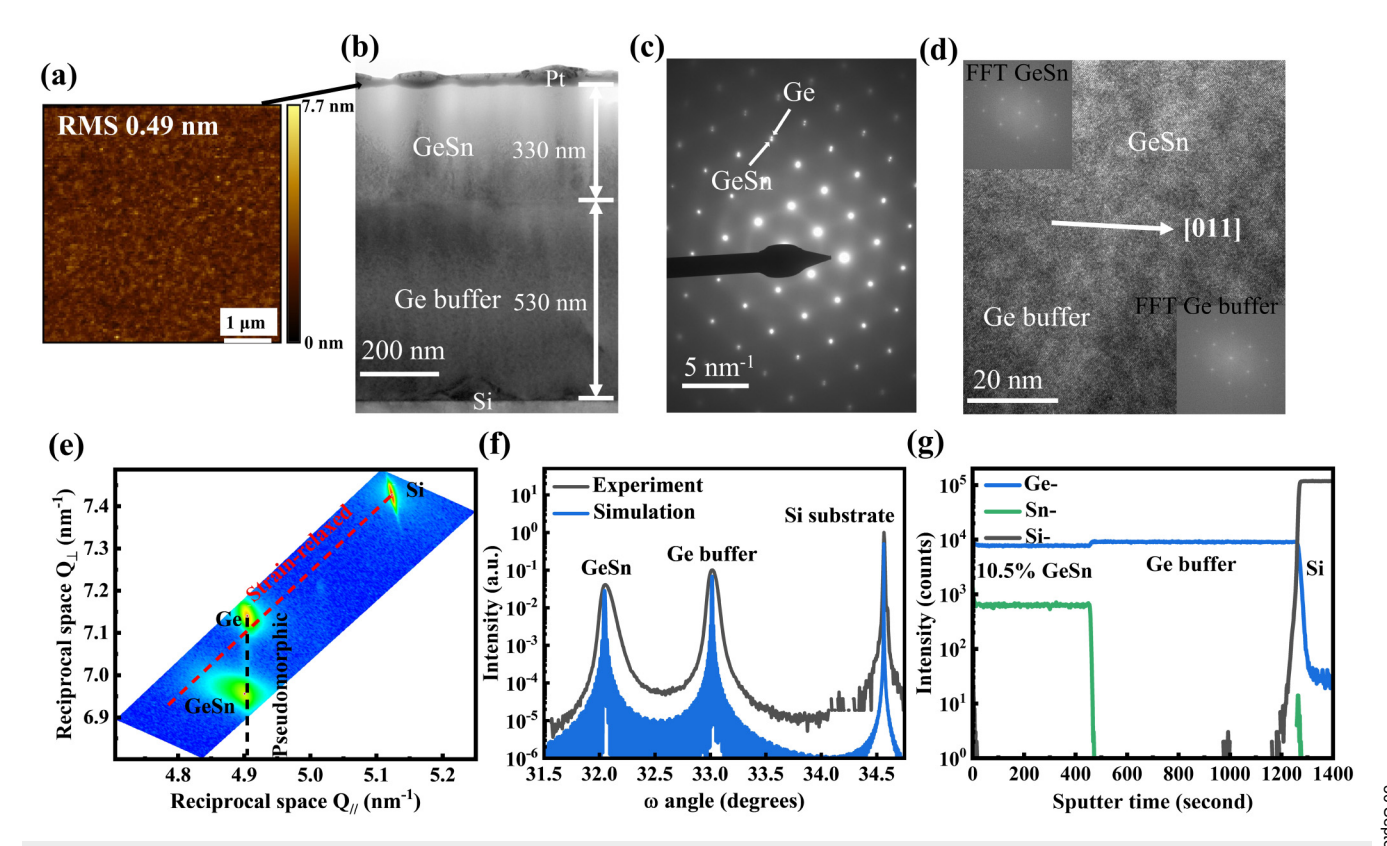


**FIG. 2.** (a) Surface morphology of the as-grown GeSn sample taken by AFM ( $5 \times 5 \mu m^2$ ) using the tapping mode, (b) low magnification cross-sectional TEM image recorded along the [110] zone axis of the GeSn grown on a relaxed Ge/Si virtual substrate, (c) SAED pattern of the GeSn and Ge buffer layers, (d) HRTEM image of the interface area between the GeSn and Ge buffer layers with inserted FFT patterns, (e) RSM around the asymmetrical (224) reflection for the as-grown GeSn sample, (f) measured and simulated XRD (004)  $\omega - 2\theta$  rocking-curve scans of the as-grown GeSn sample and (g) ToF-SIMS depth profile of Ge, Sn, and Si elements from the surface to the Si substrate.

represents the full relaxation line. The Ge buffer layer peak is slightly above this line, indicating the presence of tensile strain due to the annealing process and the difference between the thermal expansion coefficient of the Ge and Si substrates. The vertical black dash line starting from Ge buffer peak in RSM indicates the pseudomorphic line. The diffraction peaks of the GeSn layer slightly deviate from the pseudomorphic line, which implies that the GeSn layer is partly relaxed with a residual compressive strain of -1.17%. The Sn content (x), in-plane strain ( $\varepsilon_{II}$ ), out-of-plane strain ( $\varepsilon_{II}$ ), and strain relaxation (R) of the GeSn and Ge buffer layers are calculated and summarized in Table I (see Sec. 1 in the

**TABLE I.** Summary of lattice constant, in-plane strain  $(\epsilon_I)$ , out-of-plane strain  $(\epsilon_L)$ , strain relaxation (R), and Sn concentration of GeSn and Ge buffer layer extracted from the XRD-RSM.

Layer#	a <sub>0</sub> (Å)	ε∥ (%)	ε <sub>⊥</sub> (%)	R (%)	Sn (%)
Ge buffer	5.6588	0.26	-0.19	106.4	0
GeSn	5.7456	-1.17	0.89	5.5	10.55

supplementary material  $^{39}$  for the detailed XRD-RSM calculation process). Measured XRD (004)  $\omega$  –20 rocking-curve scans (upper line) are also matched with the simulations (lower line) by X'Pert Epitaxy software based on the (224) RSM result, as shown in Fig. 2(f). Figure 2(g) shows the atomic distributions of Ge, Sn, and Si along the growth direction from the surface to the Si substrate. The Sn concentration in the GeSn layer is determined to be 10.48% based on the ToF-SIMS data, which is consistent with the 10.55% Sn concentration extracted from the XRD-RSM results (see Sec. 2 in the supplementary material  $^{39}$  for the ToF-SIMS calibration process for Sn composition). In addition, the distribution of Sn atoms is very homogeneous in the depth profile of as-grown GeSn films.

In order to evaluate the strain effect induced by the transfer process, Raman spectroscopy measurements are performed. Figure 3(a) shows the Raman spectra of the as-grown sample, GeSn ribbon on the SiO<sub>2</sub>/Si substrate sample after the transfer process and the Ge reference sample. The peak located between 200 and 320 cm<sup>-1</sup> in each plot involves three peaks including Ge–Ge longitudinal optical (LO) peak, Ge–Ge disorder peak, and Ge–Sn peak.<sup>34</sup> In order to reproduce the line shape of the different peaks, an exponentially modified gaussian (EMG) function fitting

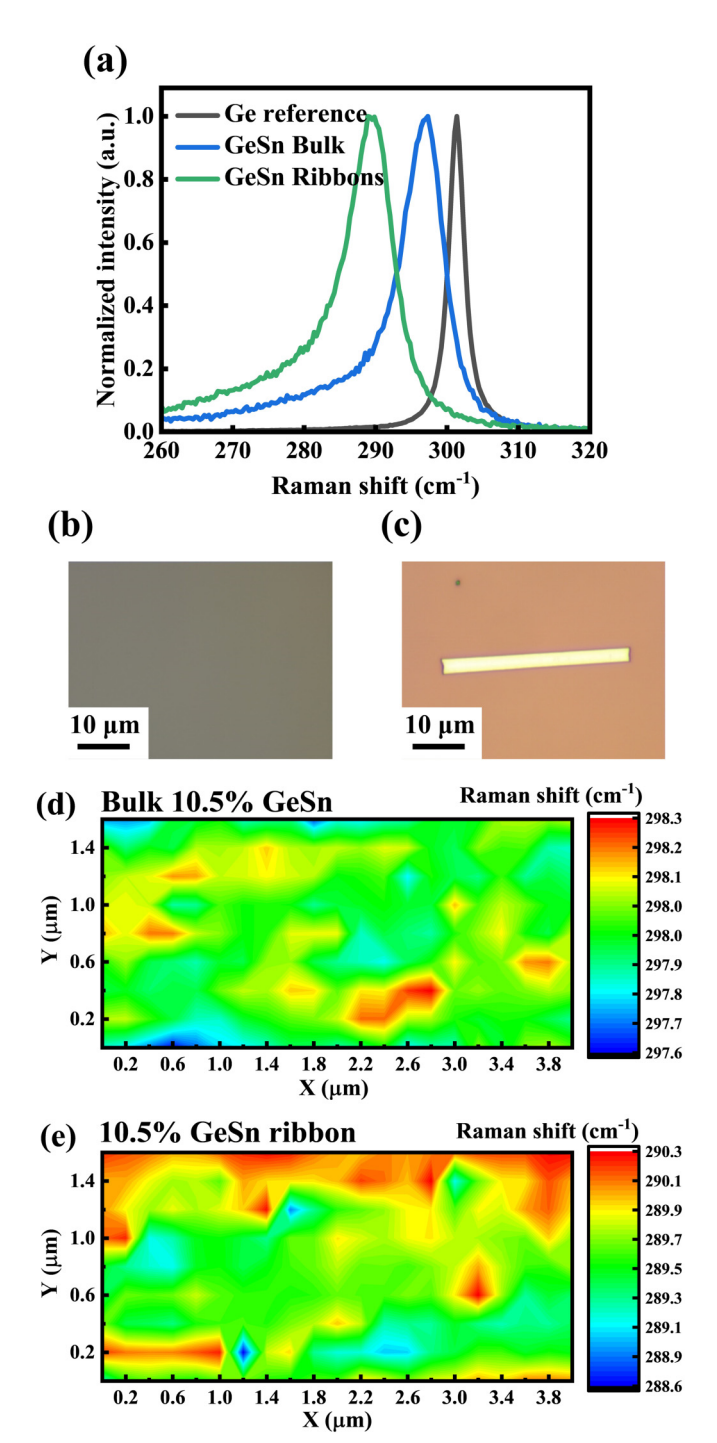


FIG. 3. (a) Raman spectrum of the GeSn ribbon compared with those of as-grown GeSn and Ge bulk samples. The Raman maps for the Ge-Ge LO mode shift for (b) as-grown GeSn sample and (c) transferred GeSn ribbon on the SiO<sub>2</sub>/Si substrate sample. The corresponding optical images of (d) as-grown GeSn samples surface and (e) transferred GeSn ribbon on the SiO<sub>2</sub>/Si substrate sample surface.

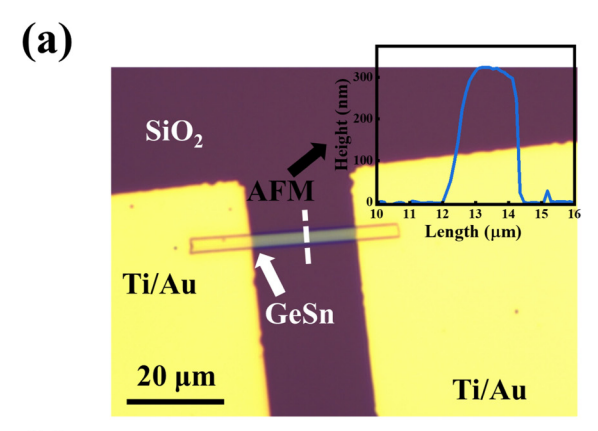
procedure is used to distinguish between the Ge-Ge LO, Ge-Ge disorder and Ge-Sn peak<sup>34</sup> [see Figs. S2(a) and S2(b) in the supplementary material<sup>39</sup> for the fitted Raman curves of the as-grown sample, GeSn ribbon on the SiO<sub>2</sub>/Si substrate sample]. The Ge-Ge LO peak position is shifted from ~297 (as-grown sample) to ~289.5 cm<sup>-1</sup> (GeSn ribbon) after the whole transfer process. The strain relaxation of the GeSn layer can be calculated according to the Raman shift value by the following equation:<sup>3</sup>

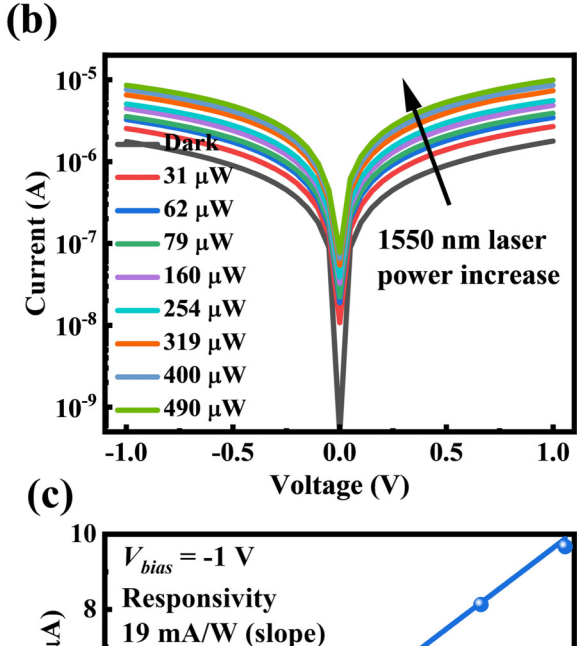
$$\Delta\omega_{\rm strain} = b\Delta\varepsilon_{//},$$

where  $\Delta\omega_{\rm strain}$  is the peak shift of the Ge-Ge LO mode associated with in-plane strain change  $\Delta \varepsilon_{\parallel}$ , and  $b = -(521 \pm 15) \text{ cm}^{-1}$  is a Raman-strain shift factor. It can be observed that the Ge-Ge LO mode shifts by ~7.5 cm<sup>-1</sup>, indicating that the strain changes from -1.17% (RSM calculated value) to +0.27%, which indicates significant strain relaxation and even change from a compressive to a tensile strain. This tensile strain effect is also seen in other studies on GeSn membranes on the  $SiO_2/Si$  substrate, <sup>25</sup> and it may arise from the interface between SiO2 and GeSn. As a result, a nearly stress-free GeSn ribbon on the SiO<sub>2</sub>/Si substrate is fabricated. Raman mapping measurements are also performed to explore the staining effect on a larger scale. The Raman maps recorded at the Ge-Ge LO peak position for as-grown and ribbon samples are displayed in Figs. 3(b) and 3(c). Figures 3(d) and 3(e) show the optical image of the as-grown and ribbon samples selected for Raman mapping. The Raman mappings are scanned over an area of  $1.6 \times 4 \,\mu\text{m}^2$  with a step size of  $0.2 \,\mu\text{m}$  (a total of 189 points per  $\approx$ sample) [see Figs. S2(c) and S2(d) in the supplementary material<sup>35</sup> for the Raman spectra of each point]. From these two mappings, it can be observed that the deviation of the Ge-Ge LO mode peak position value after the EMG fitting ranges from 0.7 to 1.7 cm<sup>-1</sup>. The increase in the deviation of the peak position of the Ge-Ge LO mode may be due to the inhomogeneity of the strain in the GeSn ribbons on the SiO<sub>2</sub> surface. During the transfer process of separat- $\overline{\infty}$ ing GeSn from Ge, minor surface roughness arises due to selective wet etching. This discrepancy in roughness between the etched back surface of GeSn and the SiO2 surface upon contact may induce additional strain. Assuming that Sn concentration remains constant compared to the as-grown sample, the tensile strain ranges from 0.22% to 0.54%.

#### B. Electrical and photoelectrical characterization

Figure 4(a) shows an optical microscope plan view of a GeSn ribbon PD device. The thickness of the GeSn ribbons is measured by AFM to be about 300 nm [as shown in the inset in Fig. 4(a)], which is slightly lower than as-grown GeSn layer thickness (~330 nm) due to the transfer etching process. In order to investigate the photoresponse of the fabricated GeSn ribbon PDs, current-voltage (I-V) characteristics under dark and light conditions are measured as shown in Fig. 4(b). The device is irradiated with a fiber guided 1550 nm laser while the bias voltage is sweeping between -1 to 1 V. The excitation is performed at different incident laser powers ranging from 31 to 490 µW. As the light intensity increases, the current is significantly enhanced. Figure 4(c) shows the plot between the photocurrent at -1 V as a





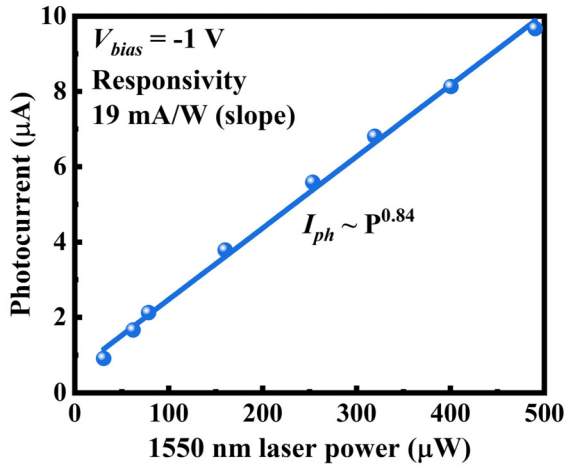
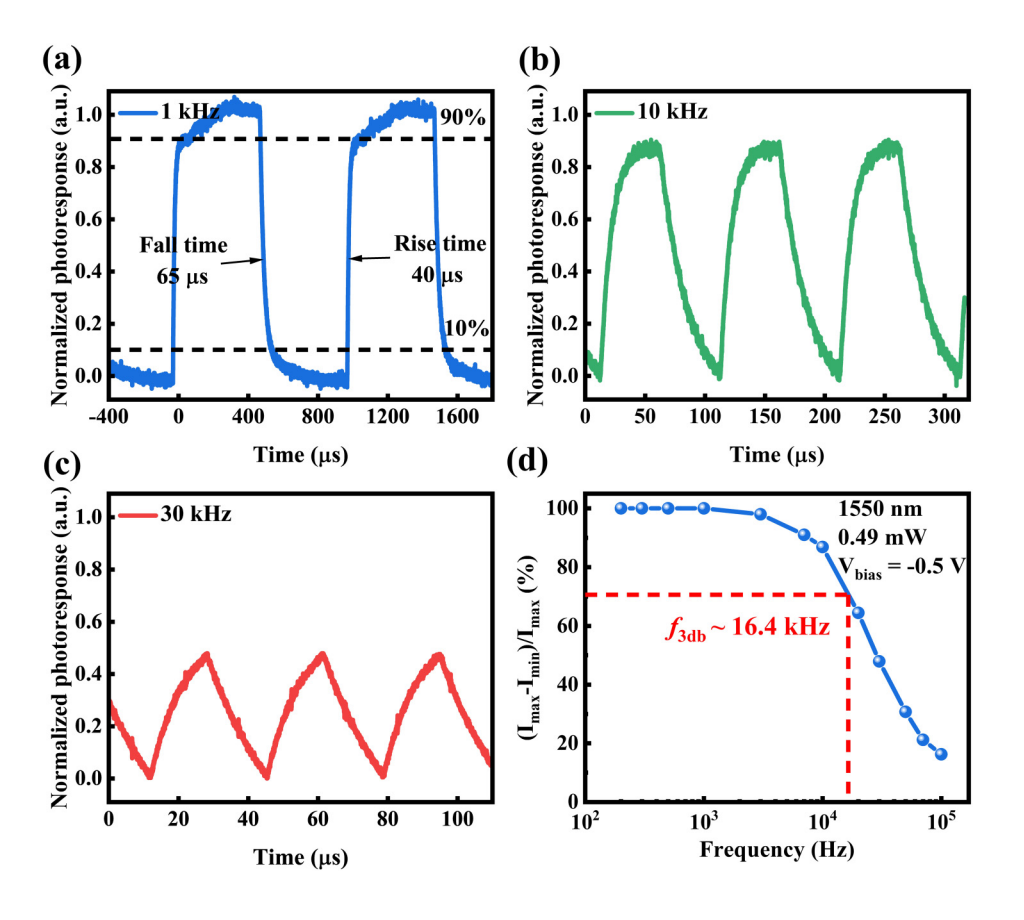


FIG. 4. (a) Optical plan view image of one fabricated GeSn ribbon MSM PD (the inset is AFM measurement of the GeSn ribbon thickness), (b) I-V characteristics of the GeSn ribbon MSM PD under room temperature under 1550 nm light illumination with powers of 0 (dark) to 490  $\mu$ W, and (c) both photocurrent and responsivity of the as-grown GeSn MSM PD as a function of 1550 nm laser power under −1 V under room temperature.

function of incident laser power. In addition, the photocurrent (I<sub>ph</sub>) is defined as the difference between  $I_{\rm light}$  (current under light conditions) and I<sub>dark</sub> (current under dark conditions). It is observed from Fig. 4(c) that I<sub>ph</sub> increases nonlinearly with the increasing laser power at -1 V. The relationship between  $I_{ph}$  and laser power can be well fitted by  $I_{ph} \propto P^{\alpha}$ , where  $\alpha$  is the fitting exponent and the fitting exponent  $\alpha$  is 0.84. The value of 0.84 is very close to the value of an ideal photodetector ( $\alpha = 1$ ), which indicates that the incident photon can be effectively converted into photocurrent. Figure 4(c) also shows the values of the responsivity at different laser powers. The responsivity can be calculated by dividing Iph by the incident laser power. As the laser power increases from 0 to  $490 \,\mu\text{W}$ , the 1550 nm responsivity decreases gradually from 30 to 17 mA/W and stabilizes at 17 mA/W.

The response speed of a PD reflects its ability to monitor rapidly changing optical signals, which is an important performance metric for PDs. Therefore, we investigate the optical response of GeSn ribbon metal-semiconductor-metal (MSM) PDs to chopped optical signals of different frequencies. A 1550 nm tunable laser with an internal chopping mode is used to generate pulsed 1550 nm laser light signals at different frequencies. The 1550 nm laser light at different frequencies is irradiated into the device through a fiber optic guide. The generated pulsed optical signals are recorded and output by an oscilloscope. Figures 5(a)-5(c) depict the temporal optical response of the GeSn ribbon MSM PD to pulsed optical signals with frequencies of 1, 10, and 30 kHz, respectively. For pulsed optical signals at a frequency of 1 kHz, the device responds quickly to laser pulses and exhibits perfect stability and reliability but g shows significant attenuation at the higher frequency of 30 kHz. The response speed can be evaluated by analyzing the rise and fall times, which are the time intervals during which the optical signal of the device rises (decays) from 10% (90%) to 90% = (10%) of the maximum optical signal of a single optical response cycle under modulated light irradiation. As shown in Fig. 5(a), the rise and fall times of the GeSn MSM PD are 40 and 65 µs at 1 kHz, respectively. To further explore the application of the GeSn MSM PD for higher-frequency optical detection, the relative balance (defined as  $[(I_{max} - I_{min})/I_{max}])$  is measured shown in Fig. 5(d), and a high 3 db frequency ( $f_{3db}$ ) of 16.4 kHz is deduced. In addition, there is some response even at frequencies as high as 10<sup>5</sup> Hz, indicating that the GeSn ribbon MSM PD is capable of detecting ultrafast optical signals. The comprehensive performance of the GeSn ribbon MSM PD is superior to that of recently reported Ge or GeSn-related PDs for SWIR detection, as summarized in Table II.

In order to better compare the performance of the GeSn as-grown and GeSn ribbon MSM PDs, we also perform the same 1550 nm measurements on the fabricated GeSn as-grown MSM PDs (see Fig. S3 in the supplementary material<sup>39</sup> for detailed information on the performance of the GeSn as-grown MSM PDs). Both GeSn as-grown and GeSn ribbon PDs show ohmic contact behavior under dark conditions. From the Ohmic behavior of dark current in GeSn as-grown and GeSn ribbon PDs, the specific resistivity R<sub>c</sub> of the device contacts are determined from transfer length measurements (TLM) (see Fig. S4 in the supplementary material<sup>3</sup> for the TLM measurement results). The TLM measured results



**FIG. 5.** Temporal optical response of GeSn ribbon MSM PD devices with a voltage bias of  $-1\,\mathrm{V}$  to chopped 1550 nm laser sources with different frequencies of (a) 1, (b) 10, and (c) 30 kHz, and (d) relative balance of  $[(I_{\text{max}} - I_{\text{min}})/I_{\text{max}}]$  as a function of frequency from 200 Hz to 10 kHz.

reveal that  $R_c$  has increased from 25.71 (as-grown GeSn) to 39.42 ohm mm (GeSn ribbons), which may be caused by the increase in the surface roughness due to the transfer etching process. Figure 6(a) shows the  $I_{dark}$  and  $I_{light}$  versus voltage for the GeSn as-grown PDs and the GeSn ribbon PDs irradiated by a 1550 nm light source at a constant power of 0.5 mW. It is observed that the  $I_{dark}$  of GeSn ribbon MSM PD is nearly 3 orders of magnitude lower than that of GeSn as-grown MSM PDs, which is most

likely caused by the difference in device footprint, as shown in  $\frac{2}{5}$  Fig. 4(a) and Fig. S3(a)<sup>39</sup>. Considering the huge difference in the  $\frac{2}{5}$  two types of PD footprints (~280×), a direct comparison of the dark currents is not very meaningful. For a fair comparison, the currents normalized by the photodetection area of each device are presented in Fig. 6(b). The normalized dark current of the GeSn ribbon PD is a bit lower than that of the GeSn as-grown reference PD. The results indicate that the electrical property of the GeSn

**TABLE II.** Comparison of the performance between this work and other similarly reported GeSn or Ge-related PDs. MSM is the photoconductor of the metal-semiconductor-metal structure, HJ is the heterojunction structure, and PIN is the photodiode of p-i-n structure.

Material	Device structure	Sn (%)	Responsivity	Response time	Cutoff wavelength (nm)
MoSe <sub>2</sub> /GeSn/Ge <sup>11</sup>	НЈ	17.1%	~3 A/W@1550 nm, 2 V at RT	462 μs	2400
Ge/GeSn/Ge <sup>12</sup>	PIN	11%	0.245 A/W@2000 nm, -1 V at RT		2650
GeSn nanowire/TiO <sub>2</sub> <sup>13</sup>	HJ	6.6%	0.245 A/W@1550 nm, -1 V at 77 K	8.3 ms	1800
GeSn membrane <sup>16</sup>	MSM	4.3%	90 mA/W@1700 nm, 5 V at RT	1.27 ms	2000
GeSn membrane <sup>25</sup>	MSM	17%	1 mA/W@2000 nm, 1 V at RT	_	4600
GeSn membrane <sup>32</sup>	MSM	8%	1.03 mA/W@2000 nm, 2 V at RT	_	>2000
Ge membrane <sup>36</sup>	PIN	0%	~50 mA/W@1550 nm, -1 V at RT	2.2 ms	>1600
GeSn/TiN <sup>37</sup>	HJ	8%	0.148 A/W@1550 nm, -2 V at RT	_	2000
GeSn ribbon (This work)	MSM	10.5%	17 mA/W@1550 nm, -1 V at RT 43 mA/W@2000 nm, -1 V at RT	$40\mu\mathrm{s}$	3200

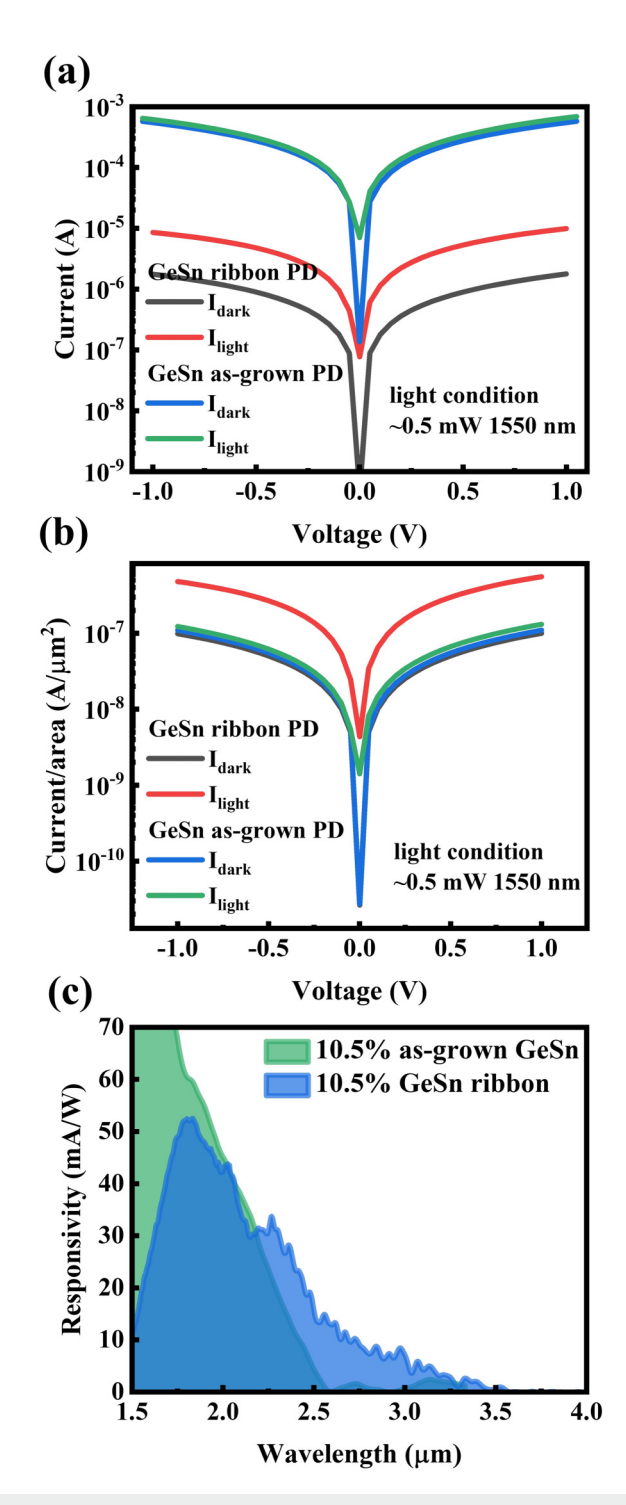


FIG. 6. (a) I-V curves, (b) normalized current (current/photodetection area) of the GeSn as-grown PD and GeSn ribbon PD under dark conditions and 1550 nm light illumination at a constant power 0.5 mW, and (c) spectral response of the GeSn ribbon MSM PD and the GeSn as-grown MSM PD under -1 V from 1500 to 4000 nm.

material does not change dramatically before and after the transfer. As for the  $I_{light}/I_{dark}$  ratio, the influence of the light effect on the current change can be seen very clearly from GeSn ribbon PD. In contrast, it is difficult to distinguish between Ilight and Idark for GeSn as-grown MSM PDs from Figs. 6(a) and 6(b). The ratio of  $I_{light}$  to  $I_{dark}$  increases from 1.12 to 5.56 (a fivefold improvement) under −1 V at the same laser power. The above results indicate that GeSn ribbon PDs based on the transfer process can effectively increase the  $I_{light}/I_{dark}$  ratio, thus improving the detectivity of the PDs. To quantitatively compare the performance of the fabricated devices over the entire SWIR range, the spectral responses of the GeSn as-grown MSM PD and GeSn ribbon MSM PD with 1.55 μm laser calibration are characterized in the 1.5 to  $4.0 \,\mu m$  wavelength range, as shown in Fig. 6(c) (see Fig. S5 in the supplementary material<sup>39</sup> for the Schematic diagram of the spectral response measurement setup). As shown in Fig. S3(d) in the supplementary material, <sup>39</sup> the responsivity of GeSn as-grown MSM PDs at  $1.55 \mu m$ wavelength is about 125 mW/A. The spectral response obtained from FTIR measurements is calibrated at 1.55 µm using 125 and 17 mA/W to obtain the actual spectral response. Three important features can be seen in Fig. 6(c). First, the responsivity value of the GeSn ribbon PD is severely degraded below the  $1.8 \mu m$  wavelength compared with that of the GeSn as-grown PD. The reason is that the responsivity of the GeSn as-grown PD below 1.8 µm comes partly from the underneath Ge buffer. Since GeSn ribbon PDs get rid of the Ge buffer/Si substrate completely, it is reasonable to observe a decrease in the responsivity below 1.8  $\mu$ m. Second, the cutoff wavelength of the GeSn ribbon PD is obviously extended to ~3.2 um, compared with the cutoff wavelength of 2.6 um for the geSn as-grown PD, which is attributed to the release of the compressive strained GeSn as-grown layer into the GeSn ribbon in a gest of the compressive strained GeSn as-grown layer into the GeSn ribbon in a gest of the compressive strained GeSn as-grown layer into the GeSn ribbon in a gest of the compressive strained GeSn as-grown layer into the GeSn ribbon in a gest of the compressive strained GeSn as-grown layer into the GeSn ribbon in a gest of the compressive strained GeSn as-grown layer into the GeSn ribbon in a gest of the compressive strained GeSn as-grown layer into the GeSn ribbon in a gest of the compressive strained GeSn as-grown layer into the GeSn ribbon in a gest of the compressive strained GeSn as-grown layer into the GeSn ribbon in a gest of the compressive strained GeSn as-grown layer into the GeSn ribbon in a gest of the compressive strained GeSn as-grown layer into the GeSn ribbon in a gest of the compressive strained GeSn as-grown layer into the GeSn ribbon in a gest of the compressive strained GeSn as-grown layer into the GeSn ribbon in a gest of the compressive strained GeSn as-grown layer into the GeSn ribbon in a gest of the compressive strained GeSn as-grown layer into the geSn ribbon in a gest of the compressive strained GeSn as-grown layer into the geSn ribbon in a gest of the compressive strained GeSn as-grown layer into the geSn ribbon in a gest of the compressive strained GeSn as-grown layer into the gest of the compressive strained GeSn as-grown layer into the gest of the compressive strained GeSn as-grown layer into the gest of the compressive strained GeSn as-grown layer into the gest of the compressive strained GeSn as-grown layer into the gest of the compressive strained GeSn as-grown layer into the gest of the compressive strained GeSn as-grown layer into the gest of the compressive strained GeSn as-grown layer into the gest of the compressive straine pressive strained GeSn as-grown layer into the GeSn ribbon in a nearly fully relaxed state. Third, the responsivity of the GeSn ribbon PD increases significantly beyond 2 μm. Compared with the GeSn as-grown PD, the responsivity of the GeSn ribbon PD shows a 163% improvement at 2.3 µm and a 356% improvement at  $2.5 \,\mu\text{m}$ . This drastic responsivity improvement may be attributed to the transition of GeSn from an indirect bandgap material to a direct bandgap material and substrate replacement with the strainrelease transfer process. Based on the theoretical calculations, <sup>38</sup> the E<sub>g</sub> (direct bandgap) of the fully relaxed Ge<sub>0.895</sub>Sn<sub>0.105</sub> is about 0.388 eV. Due to the presence of a slight tensile strain in the GeSn ribbons on the SiO<sub>2</sub>/Si substrate, which is found in the Raman results (Fig. 3), the true  $E_g^{\Gamma}$  value is slightly lower than 0.388 eV. The calculated value of  $E_g^{\Gamma}$  (direct bandgap) matches the measured spectral photoresponse range. The theoretically calculated values match the experimental results (spectral photoresponse and Raman), indicating that GeSn has been converted from an indirect bandgap material (as-grown GeSn) to a direct bandgap material (GeSn ribbons). The finite-difference time-domain (FDTD) method is used to simulate the electric field distribution difference in two different structure-as-grown GeSn and GeSn ribbons (see Fig. S6 in the supplementary material<sup>39</sup>). The substrate replacement causes a change in the light distribution, which is one of the possible reasons for the responsivity improvement. However, there are more possible factors and reasons that could lead to an increase in the responsivity, which needs to be investigated with more experiments and simulations in the future. Considering the huge

Supervision (lead); Writing - review & editing (lead).

DATA AVAILABILITY

The data that support the findings of this study are available from the corresponding author upon reasonable request.

(equal). Yuping Zeng: Conceptualization (lead); Funding acquisi-

tion (lead); Methodology (equal); Project administration (lead);

substrate in the future. It is important to note that the fabrication process of GeSn ribbon PDs has not been well optimized and there is still a lot of room for improvement in the future, which indicates a great potential for fabricating high-performance and high-speed SWIR PDs.

difference in the footprint between the two types of PDs ( $\sim$ 280×),

it is likely that another large increase in the responsivity will be

realized if a large area of GeSn can be transferred to an insulating

#### V. SUMMARY AND CONCLUSIONS

In this study, we demonstrate broadband Ge<sub>0.895</sub>Sn<sub>0.105</sub> ribbon PDs operating at room temperature, which are capable of extending the PD cutoff range to cover the entire SWIR. We show that by controlling the lattice strain and the Sn content in the 10.5% range, PD spectra in the 1.5-3.2 μm wavelength range can be achieved. We have also established a low-cost transfer process, which can release and transfer the initially highly strained GeSn layer to a variety of host substrates, including flexible and insulating substrates. In addition, compared with the as-grown GeSn reference photodetectors, the fabricated GeSn ribbon photodetectors have a fivefold improvement in the light-to-dark current ratio. The response time of the nonoptimized device at 1550 nm was 40 us, which exceeds that of most GeSn/Ge-based devices. These results indicate that GeSn ribbons are one of the ideal candidates for high-performance, cost-effective SWIR photonic devices. In addition, our developed transfer process can be extended to fabricate other GeSn-on-insulator optoelectronic and electronics devices.

#### **ACKNOWLEDGMENTS**

This work was supported by the  $\mu$ -ATOMS, an Energy Frontier Research Center, funded by the U.S. Department of Energy, Office of Science, Basic Energy Sciences, under Award No. DE-SC0023412. The authors would like to thank Dr. Xu Feng for providing valuable input on the instrumentation and data analysis involved in ToF-SIMS depth profiling, performed with the instrument sponsored by the National Science Foundation under Grant No. DMR-2116754.

#### **AUTHOR DECLARATIONS**

#### **Conflict of Interest**

The authors have no conflicts to disclose.

#### **Author Contributions**

Haochen Zhao: Data curation (lead); Formal analysis (lead); Investigation (lead); Methodology (lead); Validation (lead); Visualization (lead); Writing – original draft (lead). Suho Park: Conceptualization (equal); Methodology (equal); Writing – review & editing (equal). Guangyang Lin: Investigation (equal); Methodology (equal). Yuying Zhang: Methodology (equal). Tuofu Zhama: Methodology (equal). Chandan Samanta: Methodology (equal). Lorry Chang: Methodology (equal). Xiaofeng Zhu: Methodology (equal). Xu Feng: Methodology (equal). Kevin O. Díaz-Aponte: Methodology (equal). Lin Cong: Methodology

- <sup>1</sup>M. Amani et al., ACS Nano. 12, 7253 (2018).
- <sup>2</sup>A. M. Hoang, A. Dehzangi, S. Adhikary, and M. Razeghi, Sci. Rep. 6, 24144 (2016).
- E. Thimsen, B. Sadtler, and M. Y. Berezin, Nanophotonics 6, 1043 (2017).
- <sup>4</sup>D. J. Naczynski, C. Sun, S. Türkcan, C. Jenkins, A. L. Koh, D. Ikeda, G. Pratx, and L. Xing, Nano Lett. 15, 96 (2015).
- <sup>5</sup>K. Lin, P. Huang, H. Li, H. H. Cheng, and G. Chang, Opt. Lett. **46**, 3604 (2021)
- <sup>6</sup>X. Zhu, S. Nelan, A. J. Mercante, B. Shopp, P. Yao, S. Shi, and D. W. Prather, Opt. Mater. Express 12, 3296 (2022).
- <sup>7</sup>S. Park, Y. Kim, P. D. Nguyen, J. Jeon, B. S. Chun, and S. J. Lee, Adv. Funct. Mater. 2309897 (2023).
- <sup>8</sup>S. Park et al., Appl. Surf. Sci. 581, 152421 (2022).
- <sup>9</sup>J. Rothman et al., J. Electron. Mater. 41, 2928 (2012).
- <sup>10</sup>G. Chang, S. Yu, and G. Sun, Sensors **23**, 7386 (2023).
- <sup>11</sup>X. Cai et al., Adv. Opt. Mater. 12, 2301724 (2024).
- 12H. Tran et al., J. Appl. Phys. 124, 013101 (2018).
- 13 G. Lin et al., Nanophotonics 12, 219 (2023).
- <sup>14</sup>N. Bhargava, M. Coppinger, J. P. Gupta, L. Wielunski, and J. Kolodzey, Appl. Phys. Lett. **103**, 041908 (2013).
- <sup>15</sup>P. Martyniuk, J. Antoszewski, M. Martyniuk, L. Faraone, and A. Rogalski, Appl. Phys. Rev. 1, 041102 (2014).
- <sup>16</sup>Y. Tai, S. An, P. Huang, Y. Jheng, K. Lee, H. Cheng, M. Kim, and G. Changa, Nanoscale 15, 7745 (2023).
- <sup>17</sup>R. Hickey, N. Fernando, S. Zollner, J. Hart, R. Hazbun, and J. Kolodzey, J. Vac. Sci. Technol. B 35, 021205 (2017).
- 18C. Xu, P. M. Wallace, D. A. Ringwala, S. L. Y. Chang, C. D. Poweleit, & J. Kouvetakis, and J. Menendez, Appl. Phys. Lett. 114, 212104 (2019).
- 19W. Dou et al., Opt. Lett. 43, 4558 (2018).
- <sup>20</sup>D. Imbrenda, R. A. Carrasco, R. Hickey, N. S. Fernando, S. Zollner, and J. Kolodzey, Appl. Phys. Lett. 119, 162102 (2021).
- <sup>21</sup>G. Lin et al., J. Alloys Compd. **915**, 165453 (2022).
- 22Y. Zhu, T. Yang, H. Ding, G. Lin, C. Li, W. Huang, S. Chen, J. Wang, and J. Xu, Appl. Surf. Sci. 656, 159673 (2024).
- <sup>23</sup>G. Lin et al., Appl. Surf. Sci. 623, 157086 (2023).
- <sup>24</sup>C. Xu, D. Ringwala, D. Wang, L. Liu, C. D. Poweleit, S. L. Y. Chang, H. L. Zhuang, J. Menéndez, and J. Kouvetakis, Chem. Mater. 31, 9831 (2019).
- <sup>25</sup>M. R. M. Atalla, S. Assali, A. Attiaoui, C. Lemieux-Leduc, A. Kumar, S. Abdi, and O. Moutanabbir, Adv. Funct. Mater. 31, 2006329 (2021).
- <sup>26</sup>H. Zhou et al., Opt. Express 28, 10280 (2020).
- **27**W. Dou et al., Sci. Rep. **8**, 5640 (2018).
- 28 S. Prucnal et al., Phys. Rev. Appl. 10, 064055 (2018).
- <sup>29</sup>A. B. Talochkin and V. I. Mashanov, Appl. Phys. Lett. **105**, 263101 (2014).
- 30N. M. Eldose, H. Stanchu, S. Das, I. Bikmukhametov, C. Li, S. Shetty, Y. I. Mazur, S. Yu, and G. J. Salamo, Cryst. Growth Des. 23, 7737 (2023).
- <sup>31</sup>S. An, S. Wu, C. S. Tan, G. Chang, X. Gong, and M. Kim, J. Mater. Chem. C. 8, 13557 (2022).
- 32 H. Zhao *et al.*, Vacuum **210**, 111868 (2023).
- <sup>33</sup>Y. Ishikawa, K. Wada, J. Liu, D. D. Cannon, H. Luan, J. Michel, and L. C. Kimerling, J. Appl. Phys. 98, 013501 (2005).

 ${\bf ^{39}}{\rm See}$  supplementary material online for XRD RSM analysis of GeSn as-grown sample, ToF-SIMS measurement setup with calibration procedure for Sn concentration, Raman curve fitting and Raman mapping point data for GeSn as-grown sample and GeSn ribbon sample, 1550 nm photo-response results of GeSn asgrown MSM PDs, TLM measurements for contact resistance study, spectral photo-response measurement setup and FDTD simulation for GeSn as-grown MSM PD and GeSn ribbon MSM PD.

<sup>34</sup>H. Zhao et al., Opt. Mater. 149, 114987 (2024).

<sup>35</sup>G. Lin, P. Cui, T. Wang, R. Hickey, J. Zhang, H. Zhao, J. Kolodzey, and Y. Zeng, IEEE Trans. Nanotechnol. 20, 846 (2021).

36S. An, S. Wu, K. Lee, C. S. Tan, Y. Tai, G. Chang, and M. Kim, ACS Appl.

Electron. Mater. 3, 1780 (2021).

<sup>&</sup>lt;sup>37</sup>S. An, Y. Liao, and M. Kim, ACS Appl. Mater. Interfaces 13, 61396 (2021).

<sup>38</sup>H. Tran et al., J. Appl. Phys. 119, 103106 (2016).